3D printable strain hardening cementitious composites (3DP-SHCC), tailoring fresh and hardened state properties

van Overmeir, A. L.; Šavija, B.; Bos, F. P.; Schlangen, E.

DOI
10.1016/j.conbuildmat.2023.132924

Publication date
2023

Document Version
Final published version

Published in
Construction and Building Materials

Citation (APA)
van Overmeir, A. L., Šavija, B., Bos, F. P., & Schlangen, E. (2023). 3D printable strain hardening cementitious composites (3DP-SHCC), tailoring fresh and hardened state properties. *Construction and Building Materials*, *403*, Article 132924. https://doi.org/10.1016/j.conbuildmat.2023.132924

Construction and Building Materials 403 (2023) 132924

Contents lists available at ScienceDirect

Construction and Building Materials

journal homepage: www.elsevier.com/locate/conbuildmat

3D printable strain hardening cementitious composites (3DP-SHCC), tailoring fresh and hardened state properties

A.L. van Overmeir [a,*], B. Šavija [a], F.P. Bos [b,c], E. Schlangen [a]

[a] Delft University of Technology, Delft, Netherlands
[b] Technical University of Munich, Munich, Germany
[c] Eindhoven University of Technology, Eindhoven, Netherlands

ARTICLE INFO

Keywords:
3DP-SHCC
Printability
Mechanical properties
3D concrete printing
Strain hardening
ECC

ABSTRACT

With the introduction of 3D concrete printing, research started on how to include reinforcement in 3D printed structures. Initial studies on the implementation of strain hardening cementitious composites (SHCC) as self-reinforcing printable mortars have shown promising results. The development of this new type of SHCC comes with additional challenges. Where SHCC by itself is already a complex material engineered to achieve specific micromechanical behaviour under tensile loading, its application in 3D printing techniques imposes even more requirements - the so-called 'printability' requirements. The question that rises for the development of this new material is how to achieve printability without losing strain hardening capacity. This paper investigates the influence of raw materials and additives, such as silica fume, limestone powder, viscosity modifying agents and water, on the fresh and hardened mechanical properties of printable SHCC, by improving on a previously developed mixture. The fresh material mixtures were subjected to slump flow tests to analyse their applicability for 3D printing. In hardened state, the mixtures were tested on their compressive strength and flexural strength to assess their potential for strain hardening capacity. Finally, two mixtures were selected for printing. The mixtures were assessed on print quality and buildability by the deployment of a buildability test. Furthermore, the printed elements were mechanically tested at 28 days, on compressive strength, flexural strength and uniaxial tensile strength and strain. It was concluded that the silica fume content and water to solid ratio are relevant variables for 3DP-SHCC optimization. The study has yielded two 3DP-SHCC mix designs that display significant strain hardening capacity and good printability properties.

1. Introduction

The 3D printing of concrete (3DCP) structures has been under development over the last decade and has accelerated over the last couple of years. All over the world research is conducted to solve the remaining challenges in 3DCP. One of the most distinct challenges is the reinforcement of the printed element. Traditionally, reinforced concrete uses steel reinforcing bars to prevent the concrete from brittle failure. In the application of 3DCP the implementation of steel rebars is not trivial, and thus alternative reinforcement methods are being developed.

One of the alternative research trajectories is the development of 3D printable strain hardening cementitious composites (3DP-SHCC). SHCC, also known under the name ECC (engineered cementitious composite) is a relatively new kind of fibre reinforced material developed in the early 90's [1]. The material is characterised by its ductility and its capacity to show strain hardening behaviour under uniaxial tensile loading. These features are made possible by incorporating high-strength fibres into the cement matrix. The fibres are able to dissipate the fracture energy and distribute the cracks that form in the cement matrix as the material is stressed, which helps to prevent brittle failure under tensile loading [2].

The mechanical concept behind SHCC is as follows: as soon as the concrete matrix develops its first initial microcrack, the fibres take over the tensile force. When the fibres manage to bridge the crack, the force equilibrium of the concrete element is restored. When the force increases further, the concrete will crack at a different location, and there the same mechanism takes place. This happens repeatedly, until the tensile force within the material is higher than the fibre bridging capacity of the already formed cracks. At that moment the crack will localize, and the material finally fails. For a material to display this mechanism, it must comply with two micro-mechanical requirements:

* Corresponding author.
E-mail address: a.l.vanovermeir-1@tudelft.nl (A.L. van Overmeir).

https://doi.org/10.1016/j.conbuildmat.2023.132924
Received 12 May 2023; Received in revised form 7 August 2023; Accepted 8 August 2023
Available online 31 August 2023

Strength requirement:

$$\sigma_{tensile,fibres} > \sigma_{tensile,matrix} \quad (1)$$

The strength requirement states that the matrix cracking strength should be lower than the maximum fibre bridging capacity of the existing cracks [1].

Energy requirement:

$$Jb > Jtip \quad (2)$$

The energy requirement describes the energy balance in the crack extension process. It ensures that the fibre is able to build up enough complementary energy that it can bridge the matrix crack. When the fibre/matrix interface is too weak, the fibres are pulled out, but when the interface is too strong, the fibres break. In both cases the complementary energy will be too low to create a steady state crack and the composite will likely show strain softening behaviour. For strain hardening behaviour it is essential that the fibre has just enough freedom to deform, only then can it build up a high complementary energy which is needed to get a steady state crack and therewith its strain hardening behaviour [1].

The strain hardening capacity of SHCC makes the material appealing for its application in additive manufacturing. Unlike conventional printable mortars, which tend to fail in a brittle manner under tensile loading, the unique properties of SHCC's allows it to undergo tensile strain, making it safer for structural applications. Normally, 3D concrete printing designs focus on elements subjected solely to compressive stresses during their service life to ensure structural integrity [3]. However, one of the key advantages of 3D concrete printing is the potential reduction of material usage through design optimization [4–6]. By incorporating SHCC with its tensile strain hardening capacity, the freedom of design in 3D concrete printing can be significantly enhanced, promoting more material-efficient construction methods.

Furthermore, 3DP-SHCC can give solutions for reinforced printed elements. Currently, printed concrete structures often rely on post-tensioning systems for reinforcement [7,8]. While this generates beneficial compressive stresses in the printed concrete, it also introduces tensile splitting stresses perpendicular to the direction of reinforcement [9]. For such specific structural elements, SHCC emerges as a compelling material candidate due to its ability to withstand the tensile splitting forces arising from prestressing, thereby ensuring the structural integrity.

In addition to post-tensioned reinforcement, alternative research on reinforcing methods of 3D printed concrete elements is still ongoing. A recent study by Hass et al. [10] examines the performance of automated integrated helical reinforcement within 3D printed structures. Previous research has shown that SHCC can improve the bond with existing rebars due to the confinement effect of the fibre bridging capacity [11–13,62]. With the upscaling of reinforcement within 3D printed structures, SHCC can play a pivotal role not only by optimizing the performance of reinforcing rebars but also in enhancing the durability of these reinforced structural elements, thanks to the reduced crack width attributed to SHCC.

Several studies have investigated the implementation of SHCC as a 3D printing material [14–17]. Although printing systems and printing materials differ strongly between these studies, they have shown the high potential for SHCC as a group of self-reinforcing printable materials [18].

However, the design of 3DP-SHCC still poses several challenges. Besides the strength and energy criteria imposed by the desired strain hardening capacity, the printing process imposes additional requirements on the material. In general, the material should comply with four requirements: pumpability, extrudability, buildability and open time. Among these, the pumpability requirement (meaning that it should be fluid enough to be pumped through the printing system) and the buildability requirement (meaning that the material must be strong enough to sustain its self-weight and the weight of additional layers after extrusion) are posing contradictory demands on the fresh material properties.

Recent research has highlighted the complexity of this subject. Figueiredo et al. [15,19] focussed on the tailoring of rheological properties of a known and well-performing SHCC mix design. After the adjustment of the fresh material properties using additives and adjusting the water to cement (w/c) ratios, it satisfied the requirements of pumpability, extrudability, and open time. However, it proved to be insufficient with regard to the buildability, see Fig. 1a. Additionally, due to the adaptation of the fresh mechanical properties, the strain hardening capacity of the composite in the hardened state had been compromised. A recent publication of van Overmeir et al. [17] indicated the difficulty to comply with all the required mechanical properties. In that research, the 3DP-SHCC mixes were designed with an optimized particle size distribution to ensure good particle packing and sufficient buildability. Although some samples showed clear strain hardening capacity, the mechanical tests revealed that the composite's matrix was too strong to ensure robust strain hardening capacity. In general, PVA reinforced strain hardening cementitious composites have a compressive strength of approximately 40 MPa after 28 days [14,18,20–22]. However, the two mix designs presented in our previous publication resulted in a compressive strength that was 25% higher, with average compressive strengths of 51 and 56 MPa.

Furthermore, the improvement in buildability resulted in a reduction of pumpability and print quality. One of the issues that was found was the arching phenomenon [23,24] that occurred in the hopper of the pump. From bulk material handling, this phenomenon is known to occur in funnels and hoppers. In the current paper, the term arching refers here to the spontaneous formation of an arch-like supported mass of bulk material in a reservoir pump during gravitational flow. If a material has a high initial yield stress or presents high thixotropic behaviour, it may not flow down in the reservoir at the moment that the material underneath is transported toward the rotor–stator by the transport screw (also known as dosing screw). Instead, the bulk material will form a self-supported arch, and no material will be transported towards the rotor–stator, resulting large air voids, under extrusion, and ultimately source material depletion.

Secondly the print quality was reduced, as a result of over-extrusion. This phenomenon has repeatedly been reported for 3DCP [25,26] and is mostly observed during the printing of corners and other curved sections. Over-extrusion occurs when the volumetric flow rate of the material is too high for programmed robot speed. However, here, over-extrusion was observed irregularly during the printing of straight lines, see Fig. 1b. Therefore, it can be concluded that the reduced print quality was due to inconsistent material flow which can result from variations in viscosity due to temperature change or from irregular pumping rates due to arching effects.

The current study aims to further optimize the 3D printable mix design that was published earlier by the authors [17]. The research methodology was based on insights obtained from this prior study which highlighted two main issues. Firstly, the high initial yield stress adversely affected the printability of the composite material. Secondly, the dense and strong composite's matrix resulted in an overly strong fibre/matrix interface, which led to a reduction in the strain hardening capacity of the composite.

Therefore, this research focusses on one hand on the reduction of the initial stiffness of the material to improve pumpability and extrudability. Simultaneously, the research aims to improve the strain hardening capacity by improving the matrix fracture toughness by reducing the fibre/matrix interface bond [1,20]. A proper fibre/matrix interface bond allows for a bigger critical opening δ_p [1] and potentially also a higher maximum bridging strength σ_0, therewith increasing the complimentary energy needed for the energy requirement (Eq. (2)).

The research consists of an extensive material survey (Phase 1) which studies the effect of different material adaptions on the

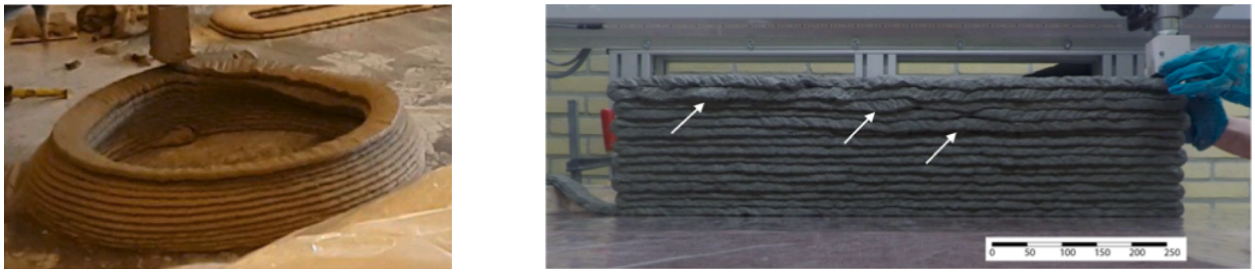

Fig. 1. a) Failure due to a combination of plastic collapse and elastic buckling [15] b) Poor print quality due to overprinting (white arrows) as a result inconsistent material flow [17].

mechanical properties in fresh and hardened state. Based on the material survey, two mix designs were selected that had the potential to produce high-quality printed objects and exhibit strain-hardening properties. These selected mixes were then subjected to further testing (Phase 2), including the 3D printing of multiple beams and a buildability test, to evaluate behaviour on pumpability, extrudability, and buildability. Samples were extracted from the printed beams and used to determine hardened mechanical properties.

2. Method

2.1. Research design

This research has been conducted in two phases. **Phase 1** covers a large experimental program on fresh and hardened state properties, to evaluate mix designs presented in Table 3. This experimental program consists of a slump flow table test, a compression test, and a 4-point bending test.

At the end of Phase 1, two mix designs (later to be renamed as Mix C and Mix D), which showed the highest potential for application in 3D Printing, were selected for further investigation.

Phase 2 consists of a cast and printed evaluation of the two selected mix designs. In cast form, the two mix designs were subjected to unconfined uniaxial compression tests (UUCT) test to evaluate the development of fresh state compression strength and Young's modulus over time, and a uniaxial tensile test, to assess the strain hardening capacity in the hardened state. For the assessment of the printed mixtures, a printing session was conducted, that consisted of a buildability test and subsequently the printing of six 5-layered beams. Test samples were extracted from the beams for the assessment of the compressive strength, the flexural strength and deflection, and the tensile strength and associated strain. An overview of the research design can be found in Fig. 2.

2.2. Materials

This research builds upon a previously designed 3DP-SHCC by van Overmeir et al. [7], herein referred to as Mix A. Mix A was acquired with a Python algorithm that optimizes the particle packing of raw materials. The algorithm was based on the modified Andreasen and Andersen (A&A) model [27] for particle size optimization and makes use of a group of boundaries conditions and input parameters (max volume, Binder/filler ratio, q-value and density specifications) [17]. Based on the mechanical and material properties, it was concluded that Mix A had potential as a 3DP-SHCC material, but further improvements on the mix design were still needed.

In a first attempt to improve the mix design, Mix A is adjusted on two aspects. Firstly, the VMA to binder ratio was reduced from 0.6% to 0.4 % to reduce the high initial yield stress which complicated the pumping phase.

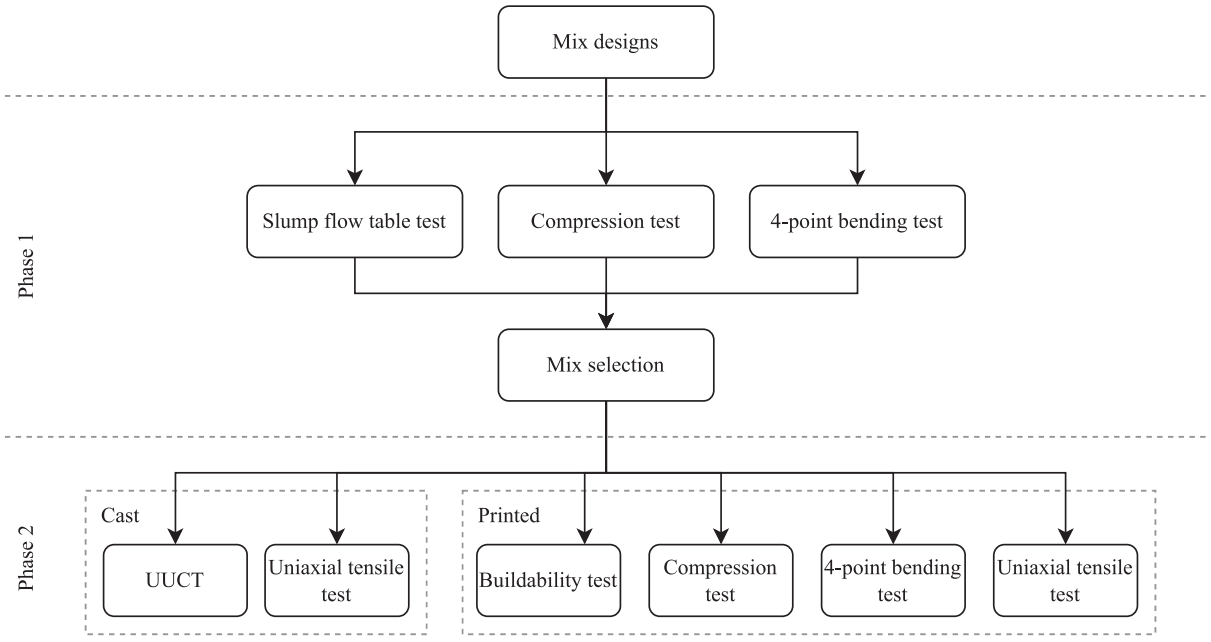

Fig. 2. Research design flow chart.

Table 1
Overview of studied parameters.

Series name	Adjustment	Range	Hypotheses
V	Reducing: Blast furnace slag (BFS)/ Limestone (LS) ratio	0.7 → 0.35	Similar PSD so it will not significantly affect the rheology, but due to the reduction of binder it is expected that it will reduce compressive strength and improve bending and strain hardening capacity
X	Reducing: Silica fume (SF)/CEM I 42,5 ratio	0.1425 → 0.0575	Reduce static yield strength and compressive strength and improve bending and strain hardening capacity
L	Increasing: Water/solid ratio	0.22 → 0.24	Reduce static yield strength and compressive strength
	Reducing: VMA/binder ratio	0.45 → 0.40	As the VMA and SP are both reduced, limited effects on the fresh and hardened state mechanical properties are expected
	SP / binder ratio	0.40 → 0.35	

Secondly, the binder to filler ratio (B/F ratio) was adapted, to reduce the matrix compressive strength and improve the strain hardening capacity of the printed elements. This was done by limiting the boundary condition related to the accepted range of B/F ratios within the modified A&A model. After rerunning the optimization algorithm this second adjustment led to a filler to binder ratio of 0.92 (where Mix A had a f/b of 0.85). When we relate this to B/F ratio to "plain" printable cement mortars, where aggregate/filler volumes fractions of 60% [28] to 75% [29] are reported, the new B/F ratio is rather low. However, the volume fractions of aggregates and fillers in SHCC are generally much lower than fibre reinforced concretes or conventional concrete, to reduce matrix toughness to comply with Eq. (2). Therefore, in this context it is more appropriate to relate this ratio to the B/F ratio of general SHCC found in literature [18] and here indeed that these ratios are well in line.

These two alterations, and the corresponding mixture composition can be found under the name Mix V in Table 3. As will be shown, these alterations caused a reduction in uniaxial compressive strength and an increase in flexural bending capacity with respect to Mix A. Mix V is therefore chosen as the starting point for this study.

In Phase 1, four mix design variables were analysed, starting with the Blast furnace slag (BFS)/Limestone (LS) ratio. Zhou et al [20] studied the BFS/LS ratio on the tensile strain hardening capacities of SHCC mixtures and showed that, as the limestone powder content increases, the compressive strength is reduced, while the flexural deflection capacity and the tensile strain capacity first increase and then decrease.

Secondly, the effect of the Silica fume to Portland cement ratio was studied. Silica fume, due to its very small particle size and spherical shape, has a strong influence on the fresh mechanical properties of cement mortars. Ferraris et al. [30] reported that the use of silica fume strongly increases the viscosity of a fresh cement mortar. Geng et al. [31] and Liu et al. [32] investigated the effect of silica fume (SF) in 3D printing mortars and found that the initial yield stress and thixotropy of the mortars increased, with increasing silica fume content. In terms of hardened properties, it is generally accepted that silica fume improves the particle packing of the mortar which leads to a denser material with a higher compressive strength [33,34]. Researchers also studied the use of silica fume in the context of SHCC. Hou et al. [35] found that the increase of silica fume content enhanced the compressive strength of SHCC with PVA fibres. However, they also concluded that excessive amounts of silica fume (>5%) resulted in loss of tensile strain capacity and an increase in the crack width. The increase in the matrix fracture toughness and alterations in fibre/matrix bond weakened the energy balance of the composite during the cracking phase, which is unfavourable for meeting the energy requirement presented in Equation (2).

The third variable was the water to solid (W/S) ratio, which strongly influences the fresh mechanical properties like static and dynamic yield stress, viscosity and thixotropy. Furthermore, an increase in W/S ratio generally reduces the compressive strength and fracture toughness [35].

Finally, the effect of a reduction in additive content was investigated. Additives, such as viscosity modifying agents (VMA) and superplasticizers (SP), are often used in SHCC [36] to optimize rheological properties and ensure sufficient fibre dispersion. In 3DCP mortars, additives are used to tailor the fresh mechanical properties with the objective to realise good printability and buildability behaviour [37]. In this research a proportional reduction of VMA and SP was investigated to see whether the amounts of additives could be reduced without affecting the fresh and hardened mechanical properties of the composite.

In Table 1 an overview is given of the variables, the range in which they were tested, and their hypothesized effect on the composite.

To limit the number of mix designs and steadily iterate towards a new printable SHCC, this research uses a "select and continue" approach where the most promising mix design of one parameter investigation was selected as the base material for the next step of the study. For example, the first parameter variation was the adjustment of the BFS to LS ratio which was investigated in the V series. The best results from this series (including mix V) were shown by mix V_2. Therefore, mix V_2 was chosen as the starting point for the X-series, in which the SF/CEM ratio was varied. A full overview of the mix iteration can be found in Fig. 3; the mixes indicated in green were selected as the base mix for the future series, the mixes indicated in bold are the materials that were chosen for the elaborate material evaluation in Phase 2.

A full overview of the material parameters can be found in Table 2, and the mix compositions can be found in Table 3.

All mixtures were prepared in volumes of 3.5 L according to the following mixing routine:

- 2 Minutes: Mixing all dry materials, including the fibres, SP and 1/3 of the VMA
- 1 Minute: Adding of water while mixing
- 1 Minute: Mixing of wet material
- Add the remaining 2/3 of the VMA
- 2 Minutes: Mixing of wet material

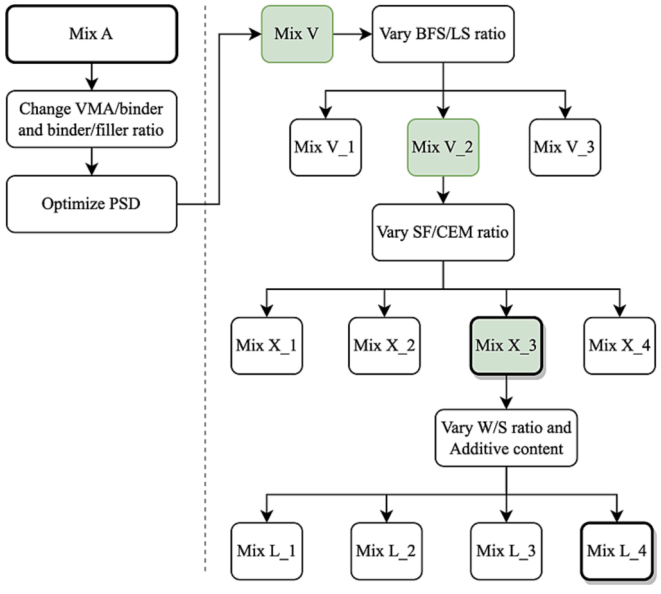

Fig. 3. Mix design flow chart (Phase 1).

Table 2
Research parameters.

	BFS/LS	SF/CEM 1	Water/Solid	VMA/binder	SP/binder
M A	0.7	0.1425	0.22	0.60%	0.40%
Mix V	0.7	0.1425	0.22	0.45%	0.40%
Mix V_1	0.55	0.1425	0.22	0.45%	0.40%
Mix V_2	0.45	0.1425	0.22	0.45%	0.40%
Mix V_3	0.35	0.1425	0.22	0.45%	0.40%
Mix X_1	0.45	0.13	0.22	0.45%	0.40%
Mix X_2	0.45	0.1	0.22	0.45%	0.40%
Mix X_3	0.45	0.07	0.22	0.45%	0.40%
Mix X_4	0.45	0.0575	0.22	0.45%	0.40%
Mix L_1	0.45	0.7	0.23	0.45%	0.40%
Mix L_2	0.45	0.7	0.24	0.45%	0.40%
Mix L_3	0.45	0.7	0.23	0.40%	0.35%
Mix L_4	0.45	0.7	0.24	0.40%	0.35%

Compared to traditional SHCC, 3DP-SHCC is a very dough-like mixture. Due to the high viscosity of the fresh slurry, it is difficult to disperse the fibres sufficiently when 100% of the VMA is added in the beginning. As sufficient fibre dispersion is essential for a robust performance of SHCC, the mixing procedure prescribes to add the VMA in two phases.

The raw materials used in this study are: CEM I 42,5N, Silica fume (SILMIX®), Blast furnace slag (ECO_2CEM), Limestone powder (Inducal 105), River sand (GEBA, D_{90} = 0.17 mm), SP (Melflux 2651F), VMA (Tylose MHS).

The mixtures were reinforced with RECS15 Poly-vinyl-alcohol fibres (PVA), supplied by Kuraray GmbH. Fibre specifications are given in Table 4.

2.3. Experiments

For all the cast and printed elements that were tested in hardened state, the same curing procedures were applied. Directly after printing the printed elements were covered with foil. After one day of curing the printed and cast elements were moved to the fog room with a temperature of 20 °C with a relative humidity of 97%. One week after casting/printing, the elements were sawn into sample size, as specified per test, after which they were placed back in the fog room. Finally, the samples were removed from the fog room one day before testing.

2.3.1. Slump flow Table test

For the assessment of the rheological properties the Slump flow table test, as specified in EN 1015–3 [38], was utilized. This test makes use of a circular rigid flow table that drops 15 times (without significant friction) over a height of 12.7 mm. The table has a weight of 4.35 kg and a diameter of 255 mm. The material is filled into a smooth cone, that has a height of 60 mm high, a top diameter of 70 mm and a bottom diameter 100 mm. The total volume of the tested material is 351.1 mm^3. The full test set-up can be viewed in Fig. 4.

Table 4
RECS15 fibre specifications.

		PVA (RECS15)
Tensile strength	MPa	1600
Modulus of elasticity	GPa	41
Ultimate strain	%	6
Length	mm	8
Diameter	µm	40
Aspect ratio	L/D	200
Density	kg/m^3	1.3

The test is performed at multiple ages to assess the reduction in workability of the fresh 3DP-SHCC mortar. Specifically, the test was caried out at t = 5, 10, 15, 20, 25 and 30 min, where t = 0 is the moment of adding of the water during the mixing procedure.

During testing, a recording camera was positioned in top-view as can be seen in Fig. 5. Subsequently, image analysis was used to accurately determine the mean spread diameter of the material. Due to the very minimal slump that these materials show directly after lifting of the mould, this parameter was not included for analysis within this research.

A variation of this test principle has been utilized by Cho et al. [39] to test fresh mixtures on their applicability for 3D printing. In their assessment they concluded that mortar is printable when the diameter stays within the range of 130–180 mm. They suggested that materials with a larger diameter after testing will result in insufficient buildability. Stiffer materials with a spread diameter < 130 mm are likely to be difficult to pump and to result in reduced printing quality such as filament tearing. It must be noted that Cho et al. conducted their research

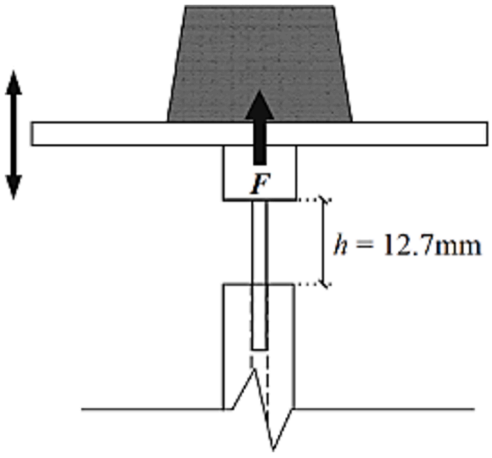

Fig. 4. Slump flow table test setup [39].

Table 3
Material composition [g/dm^3].

	BFS	***CEM I*** *42.5* N	***SF***	***LS***	***Sand***	***Water***	***PVA*** (vol%)	***VMA***	***SP***
Mix A	329	506	73	468	298	364	2	5.46	3.65
Mix V	348	470	67	499	318	374	2	3.98	3.54
Mix V_1	300	470	67	546	318	374	2	3.77	3.35
Mix V_2	263	470	67	584	318	374	2	3.60	3.20
Mix V_3	220	470	67	627	318	374	2	3.41	3.03
Mix X_1	263	470	61	584	318	373	2	3.57	3.18
Mix X_2	263	470	47	584	318	370	2	3.51	3.12
Mix X_3	263	470	33	584	318	367	2	3.45	3.06
Mix X_4	264	470	27	583	318	365	2	3.43	3.05
Mix L_1	263	470	33	584	318	384	2	3.45	3.06
Mix L_2	263	470	33	584	318	400	2	3.45	3.06
Mix L_3	263	470	33	584	318	383	2	3.06	2.68
Mix L_4	263	470	33	584	318	400	2	3.06	2.68

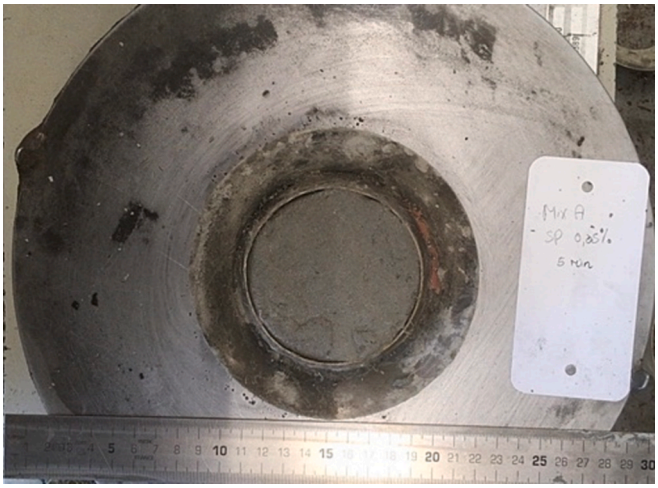

Fig. 5. Top view camara position for data processing.

according to the ASTM C230 guidelines, which has a different cone shape, resulting in a volume reduction of 16.7%. From research conducted by Shamir et al. [40], on a mini slump flow test, it is known that the changed cone type results in a smaller flow diameter with a correlation factor of 0.917. Additionally, the research conducted by Cho et al. was performed with a mortar without any fibres. Due to these two differences in experimental method, the range as suggested by Cho et al. is regarded as an indication only.

The Slump flow table test does not directly measure the yield stress of a material, but it gives an indication of the workability which can be related to the yield stress. Therefore, a concrete mixture with a high slump flow value (high spread diameter) is considered to have a low yield stress and vice versa.

Additionally, the test does not supply information on the thixotropy of a material; two materials with the same slump flow can result in significantly different building heights. Models to correlate slump tests [41] and Slump flow table tests [42] to the static and dynamic yield stress have been proposed, but will not be regarded in the context of this study.

2.3.2. Compression test and apparent density

The assessment of the compressive strength took place 28 days after the casting and the printing of the samples. The cubed samples with an edge of 35 mm (±1 mm) were measured and weighed prior to testing to determine their apparent density. The test was conducted in a servo-hydraulic machine and performed in accordance with ASTM-39 [43] with a constant load rate of 2.0 kN/s. The printed samples were tested in orientation ***w*** (load perpendicular to printing plane) and orientation ***v*** (load perpendicular to the printing direction), as defined by the RILEM Technical committee ADC (Assessment of Additively Manufactured Concrete Materials and Structures) [44]. The values that are displayed in the result section are the averages of six samples, for both the cast and the printed samples.

2.3.3. 4-point bending test

The 4-point bending tests were performed to determine the flexural strength and associated deflection of the cast and printed samples at an age of 28 days. The test samples have a size of 30 mm (b) × 8 mm (h) × 150 mm (l) (±1 mm). For the printed beams, the height of 8 mm ensures the absence of an interlayer zone within the test sample. The printed samples were tested in orientation ***v.u***, where ***v*** is the axis (perpendicular to the printing direction) around which the bending moment takes place and ***u*** the longitudinal axis of the sample, in the printing direction (in the flexural test, this coincides with the load span direction). The 4-point bending tests, with a load span of 120 mm and a span rod spacing of 1/3rd of the load span, are performed on an Instron 8872 servo-hydraulic testing system. The experiments were conducted in displacement-controlled mode at a rate of 0.01 mm/s. The effective displacement was measured during testing by employing two LVDTs that were mounted on the steel elements of the test set-up. Due to the position of the LVDTs, the measurement of the vertical displacement relates to the average displacement of the two middle rods. The test set-up can be viewed in Fig. 6.

The values that are displayed in the result section are the averages of four samples.

Note that flexural hardening capacity does not always guarantee strain hardening behaviour, but it is a prerequisite for a material to achieve strain-hardening in tensile loading. Therefore, this relatively fast test was used for initial assessment of the mix designs.

In phase 2, the average flexural toughness (T_f) of the cast and printed samples was calculated in accordance with the method proposed by Kim et al. [45]. This method is applicable for the deflection hardening behavior observed in strain hardening cementitious composites and gives an indication on the energy absorption capacity of the mix designs [46,47]. The flexural toughness of deflection hardening materials is indicative of the energy stored in the composite and can be obtained through the area under the load–deflection curve.

The flexural toughness was determined for two data points in the flexural load–deflection curves, namely, the limit of proportionality (LOP) and the modulus of rupture (MOR), where the LOP is the point at which the load–deflection curve starts to exhibit noticeable non-linearity and MOR is defined as the point where deflection softening starts to occur after the maximum load is reached.

Effectively, the flexural toughness of LOP ($T_{f,LOP}$) is the area under the load–deflection curve left of the LOP which represents the energy storage until first crack. $T_{f,MOR}$ represents the energy storage until maximum flexure load, the area left of the MOR (including $T_{f,LOP}$). All relative parameters are presented in Fig. 7. To eliminate the small variations in sample size due to the sawing of the printed materials, the average flexural toughness's was derived from normalized loads for the standard sample cross-sectional area of 30 × 8 mm^2.

2.3.4. Unconfined uniaxial compression test

The Unconfined Uniaxial Compression Test (UUCT) was used to determine the development of the fresh state compression strength and the apparent Young's modulus of the printable mix design. The method has been developed by Wolfs et al. [48], and was adapted from the traditional UUCT standard for soil specimens, ASTM D2166 [49]. This modified UUCT is well accepted in the field for the quantification of fresh properties of 3DP mortars [50–52].

The UUCT is performed on a cylindrical sample with a diameter of 70 mm and a height of 140 mm. The samples are made with the use of a steel mould covered with baking paper on the inside to avoid sticking of the fresh material. The sample is demoulded one minute prior to testing. The sample is then placed in a Instron 5967 testing system, where a 5 kN load cell with a 70 mm diameter loading plate is used to transfer the vertical compressive force onto the sample. The tests were performed in displacement-controlled mode at a rate of 30 mm/min. The material was tested over the first hour of hydration, with the time intervals: t = 10, 20, 30, 45 and 60 min, and a sample size of three samples per time interval. Here, t = 0 min is defined as the time of water addition in the mixing procedure.

During the test, the deformation of the sample is captured with an optical camera. With the use of National Instruments Vision Builder, the optical data is post-processed and the load dependent cross-sectional area is obtained. The Unconfined Uniaxial Compression Test is used to measure the initial yield strength and its change over time, by testing the mix designs at various intervals after mixing. The initial apparent Young's modulus (and its development in time) was be calculated based on the compression stress and strain of the elastic part of the stress strain curve (measured at 5% strain). The two obtained linear trendlines can,

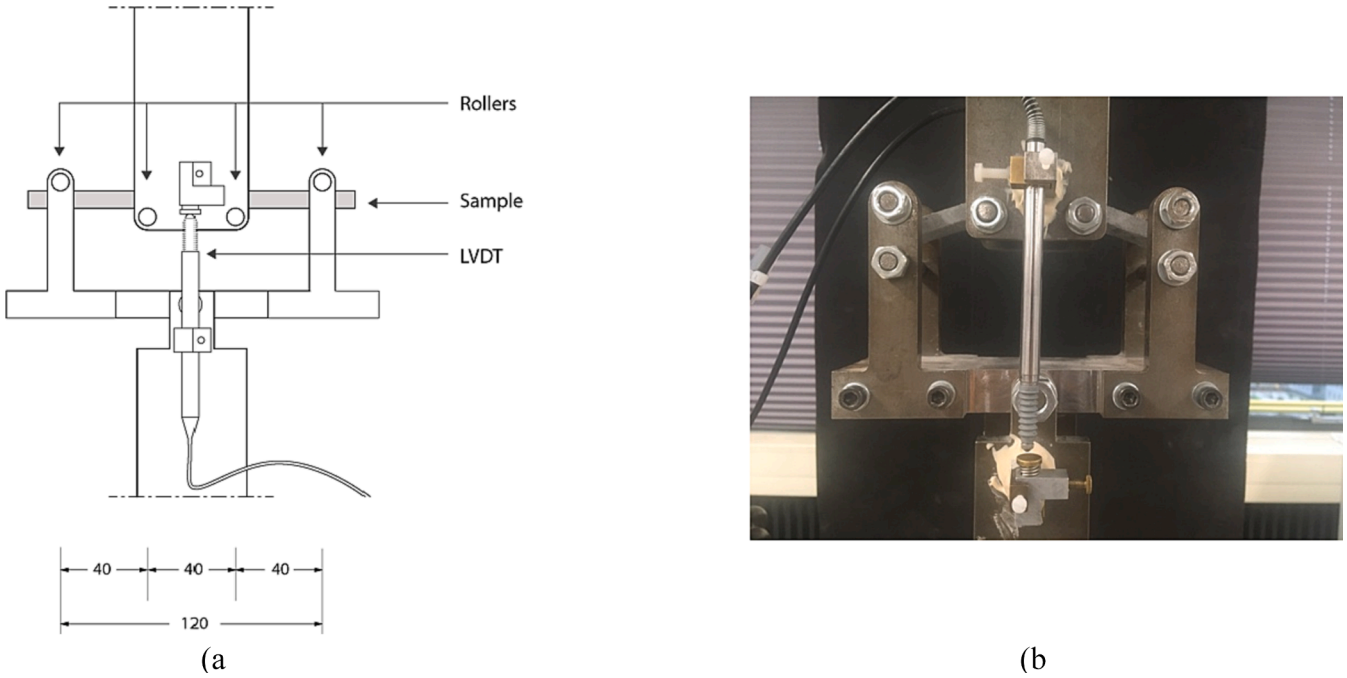

Fig. 6. 4-point bending test set-up, a) Set-up design with measurements in mm, b) Sample deformation after testing.

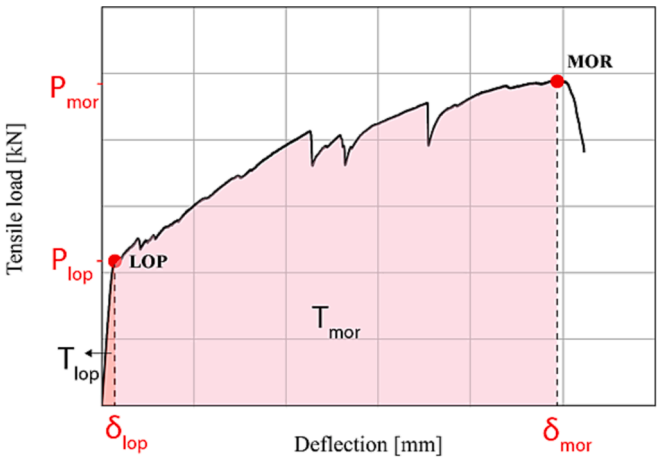

Fig. 7. Parameters used for the flexural toughness in a standard SHCC load–deflection curve.

together with the buildability model proposed by Suiker [53], be used to predict the achievable building height in a buildability test.

2.3.5. *Buildability test and printing of beams*

A buildability test was carried out by printing a slender wall in subsequent layers of 800 mm length. During the test, two cameras were orientated towards the front and the side of the wall, to register the layer-by-layer build-up until failure. Failure can occur because of plastic collapse or elastic buckling, but it has also been reported that a combination of these two mechanisms can lead to failure [48,54]. The achieved building heights were compared with the predicted heights retrieved from the UUCT.

For the mechanical tests on the printed material six beams with a height of five layers and a length of 800 mm were manufactured.

For the buildability test and printing of the beams, the gantry system 3D printer of the Eindhoven University of Technology (TU/e) was utilized [55]. For the pumping of the material, a M−Tec P20 Connect cavity pump was utilized. The pump was equipped with a D8-2 Rotor/stator capable of accommodating particles of up to a maximum size 3 mm. Furthermore, the pump reservoir was equipped with an Archimedes transport screw with an outer diameter of 90 mm and a central cylindrical shaft of 38 mm. The pump was connected to a 5-meter long hose with a 25.4 mm diameter and a downflow nozzle with a rectangular cross-section of 40 × 14 mm^2. The material was mixed in batches of 3.5 L with an A200-N Hobart planetary mixer.

Initially, a single layer filament was printed at different speeds and constant pumping pressure, whereby the width of the filaments was measured to select the optimal printing speed. Subsequently, the Buildability test was conducted, followed by the printing of the six 5-layer heigh beams. Both were printed with a back-and-forth printing routine [17].

2.3.6. *Uniaxial tensile test*

The uniaxial tensile tests were carried out 28 days after casting and printing on dog-bone-shaped samples. The dog-bone samples were acquired by casting fibre reinforced concrete 'feet' around a rectangular beam with an average size 20 mm [w] × 40 mm [h] × 250 mm [l] (±1 mm), as can be viewed in Fig. 8. For the cast samples, the rectangular beams were extracted from a bigger cast element with a size of 100 mm [w] × 100 mm [h] × 300 mm [l]. For the printed samples, the rectangular beams were extracted from a 5-layer high beam, of which the top and bottom layer were excluded. A more elaborate description on the sample preparation can be found in author's previous work [56].

Tests were conducted on an Instron 8872 servo hydraulic testing system making use of the strain-controlled mode. The displacement rate was set to 0.5 μm/s, resulting in a strain rate of 5 microstrain/s. Two LVDT sensors were utilized to measure the vertical displacement, and the average value of the LVDTs was used to control the vertical strain rate.

3. Results and discussion Phase 1

3.1. *Slump flow Table tests*

The results of the Slump flow table tests that are presented in Fig. 9 show the effect of the design parameters on the workability of the different mixes.

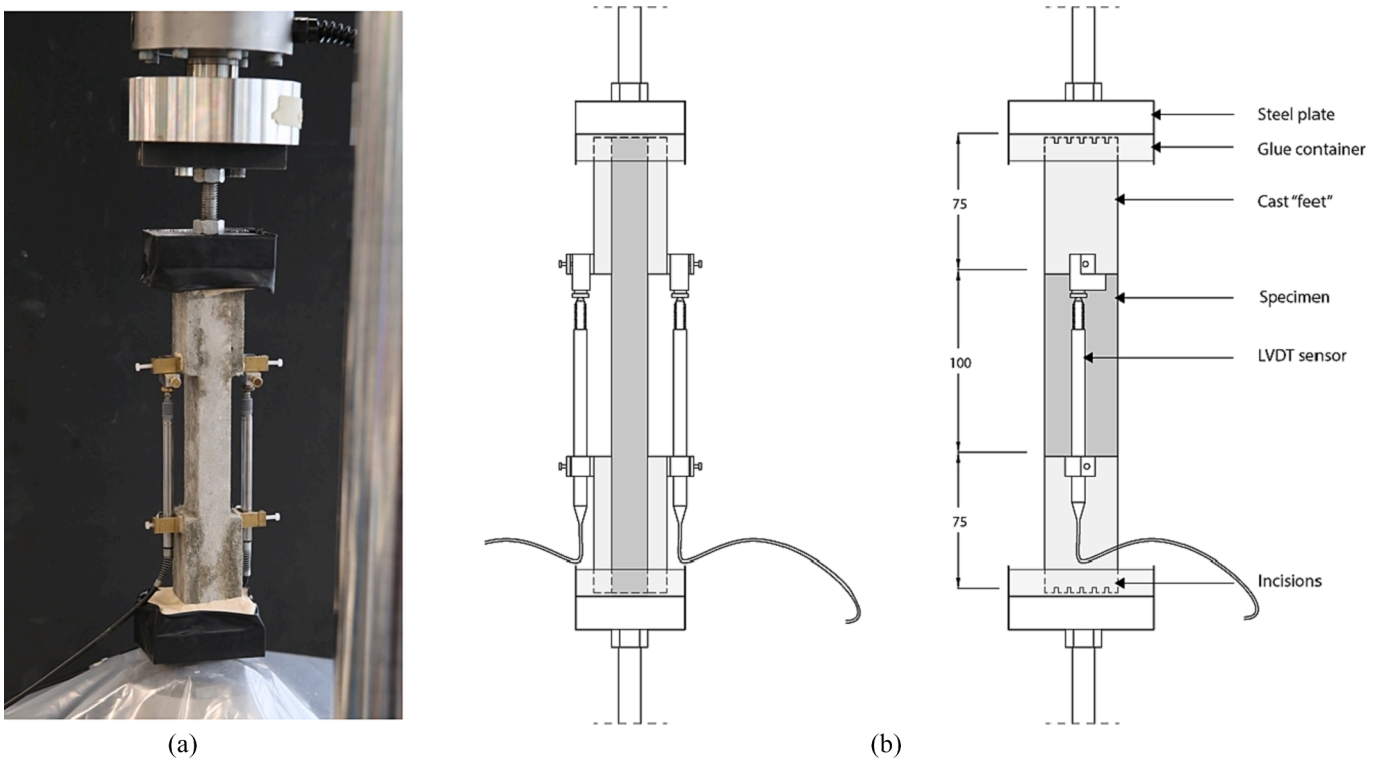

Fig. 8. Uniaxial tensile test set-up, a) Installed dog-bone sample, b) Set-up design with measurements in mm.

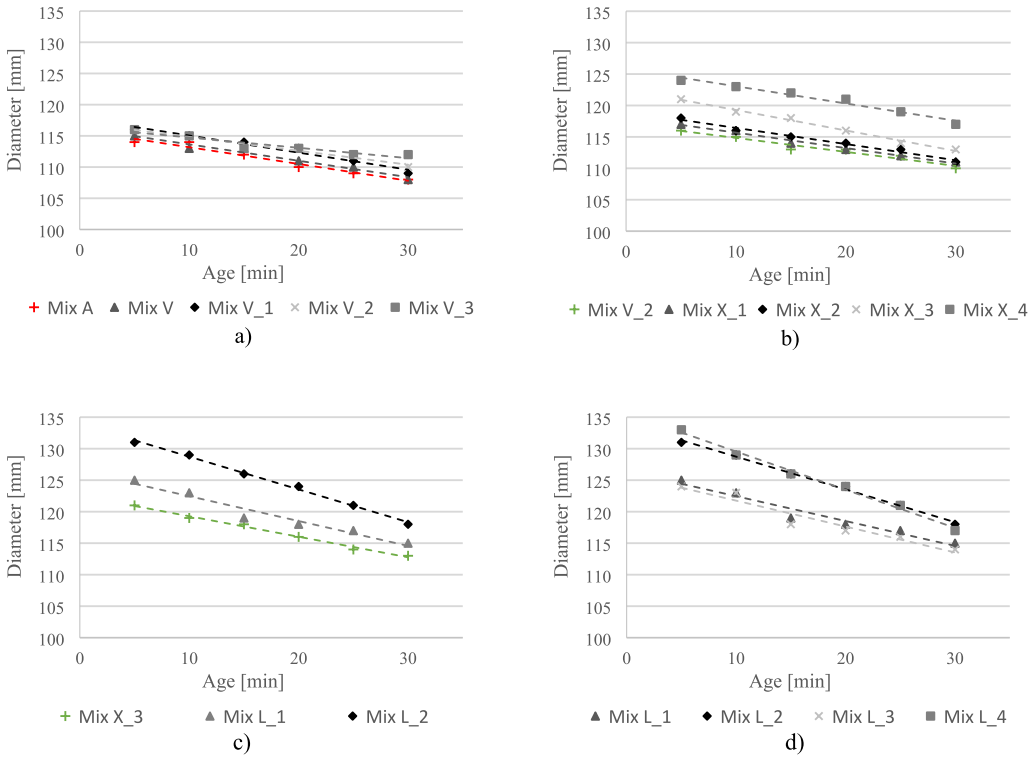

Fig. 9. Slump flow diameter of a) The V-series, b) X-series c) the L-series (W/S) and d) the L-series (Additive content), the mixes shown in green represent the selected material from the previous series, as indicated in Fig. 3. (For interpretation of the references to colour in this figure legend, the reader is referred to the web version of this article.)

The results of the V-series, namely Mix V - V_3 (BFS/LS) (Fig. 9a), confirm that adjusting the BFS/LS ratio has a limited effect on the initial flow. All mixtures, when tested directly after mixing (t = 5 min), show a diameter of ± 116 mm, meaning that the diameter of the material increased by only 16% over the course of the 15 drops. The differences between the mixtures become more pronounced when the material

becomes older. The mixtures with a high BFS/LS ratio (i.e., higher binder/filler content) show a steeper downward slope over time then those with lower BFS/LS ratios. This can indicate that early hydration products, because of the higher binder content, already affect the slump flow diameter within the first half hour.

The results of the X-series reveal that the reduction of silica fume to cement content results in an increased slump flow diameter. This suggests a decrease in the initial yield stress of the material, as supported by the literature [41,42]. In contrast to the V-series, the graphs of the X-series (Fig. 9b) remain parallel to each other, indicating that the change of silica fume content does not affect the rate at which the workability is reduced.

Within the L-series, mixes X_3, L_1, and L_2 show the results of the increasing water to solid ratio from 0.22 to 0.23 and 0.24, respectively. As anticipated, this modification significantly affected the final diameter of the Slump flow table test, with an increase of ± 4% per 0.01 increase of W/S ratio (Fig. 9c).

Upon examination of the impact of reducing the additive content (VMA and SP) in comparable proportions (i.e., L_1 vs L_3 and L_2 vs L_4), it can be concluded that there is no substantial impact on the material response to the Slump flow table test (Fig.9d). The variations observed are within the margin of error.

When the flow diameters are juxtaposed with results of Cho et al, [39], it is found that only mix designs L_2 and L_4 comply with his requirement of minimal flow conditions to achieve good printing quality.

3.2. Compression test

The compression test results with their standard deviations are presented in Fig. 10. For comparison, the results of the selected material from the previous series were included in each bar chart. All modifications of the initial Mix A resulted in a decrease in compressive strength, except for the mix designs where the VMA and SP were adjusted. For the V-Series, the compressive strength reduced from 47.93 MPa to 44.71 MPa for Mix V and Mix V_3, respectively. In the X series, the compressive strength further decreased, with a compressive strength of 46.7 MPa for mix X_1 containing a 13% silica fume to 43.5 MPa when the silica to cement ratio was reduced to 5%. The largest reduction in compressive strength was achieved through adjustment of the w/s ratio, with a decrease from 44.09 MPa (Mix X_3) to 38.69 MPa (Mix L_4).

Table 5
Average results with standard deviations of the 4-point bending tests.

	Maximum flexural stress [MPa]			Deflection at max. flexural stress [mm]		
		STD	RSTD [%]		STD	RSTD [%]
Mix A	**11.18**	± 1.41	12.6	**5.80**	± 1.13	19.5
Mix V	**8.95**	± 0.82	9.2	**8.42**	±1.39	16.5
Mix V_1	**8.81**	±1.94	22.1	**7.72**	± 1.29	16.7
Mix V_2	**9.11**	± 1.37	15.1	**8.00**	± 1.92	24.0
Mix V_3	**8.47**	± 1.02	12.0	**5.82**	± 0.71	12.2
Mix X_1	**8.98**	± 1.20	13.4	**8.87**	± 1.07	12.1
Mix X_2	**9.57**	± 1.38	14.4	**7.24**	± 1.89	26.1
Mix X_3	**10.83**	± 1.07	9.9	**9.85**	± 0.38	3.8
Mix X_4	**10.51**	± 1.24	11.8	**9.61**	± 1.29	13.4
Mix L_1	**9.53**	± 1.03	10.8	**9.78**	± 1.83	18.7
Mix L_2	**8.59**	± 0.79	9.2	**9.83**	± 1.85	18.9
Mix L_3	**8.45**	±1.00	11.8	**9.71**	± 2.25	23.2
Mix L_4	**9.02**	± 0.81	9.0	**11.91**	± 1.25	10.5

3.3. 4-point bending test

The results of the 4-point bending test conducted in Phase 1 are presented in Table 5. All the mix designs exhibited flexural hardening in orientation ***v.u***. Overall, it can be concluded that the modifications made to the mix designs resulted in a reduction of the maximum flexural

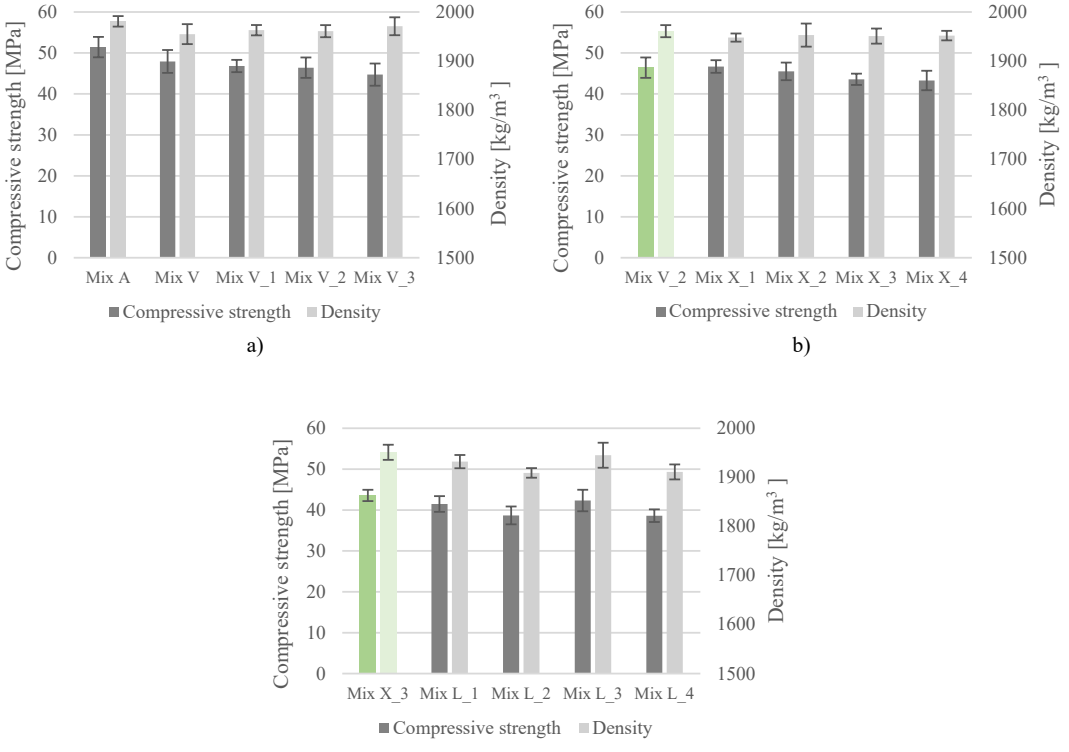

Fig. 10. Compression strength and apparent density of a) The V-series, b) X-series and c) the L-series, the mixes shown in green represent the selected material from the previous series, as indicated in Fig. 3. (For interpretation of the references to colour in this figure legend, the reader is referred to the web version of this article.)

strength and an increase of the deflection at maximum flexural stress compared to Mix A. Upon closer examination of the specific parameter series, it was noted that the modification made to the mix designs from Mix A to Mix V resulted in a significant reduction in the maximum flexural strength, as well as an improvement in the deflection capacity. Specifically, the reduction in binder-to-filler ratio resulted in a strongly reduced flexural strength from 11.19 MPa to 8.95 MPa, for Mix A and Mix V respectively. At the same time, it significantly improved the deflection capacity from 5.8 mm to 8.42 mm, an increase of 45%.

The results of the V-series show that the adjustment of the BFS/LS ratio has limited influence on the flexural strength of the composites. The flexural strength displayed a minimal reduction from 8.95 MPa to 8.47 MPa for Mix V (BFS/LS = 0.7) and Mix V_3 (BFS/LS = 0.35), respectively. In line with the findings of Zhou et al. [20] the deflection capacity decreased for Mix V_3, the mix design with the highest limestone powder content. Where Mix V-V_2 displayed deflection capacities around 8 mm ± 0.35. Mix V_3 achieved an average deflection of 5.82 mm.

The X-series, with reduced silica fume-to-cement ratio, shows a clear improvement in flexural strength and deflection capacity. Mix X_3 and Mix X_4 exhibit similar flexural properties, with a strength of 10.65 ± 0.18 MPa and a deflection capacity of 9.7 ± 0.15 MPa. However, Mix X_3 stands out with low RSTD values of 9.9% and 3.8%, respectively. The decrease in silica fume content likely led to a lower matrix density and weakened the bond between fibres and the matrix.

The mechanical properties acquired from the L-series, show that the increase of w/c ratio directly affects the flexural strength of the material, reducing from 10.83 MPa for Mix X_3 (w/c = 0.22) to 8.59 MPa for Mix L_2 (w/c = 0.24). Interestingly the results show that the flexural deflection capacity was not affected by the w/c ratio. The highest deflection capacity was found for Mix L_4, with a deflection at maximum stress of 11.91 mm.

Overall, when the results of the 4-point bending tests are related to the compressive strength results, it can be concluded that samples with reduced compressive strength display a higher flexural deflection capacity. It is expected that the theory of Hou et al. [35] applies here. The theory states that the lower compressive strengths relate to lower matrix fracture toughness, which can improve the energy balance in the crack extension process.

3.4. Conclusions Phase 1

The main objective of Phase 1 was to improve the material properties of 3DP-SHCC by adjusting 4 parameters subsequently. From the experimental results the following conclusions can be drawn.

- The BFS/LS ratio adjustment (V-series) has no significant influence on the workability of the fresh material directly after mixing. However, it has been shown that this adjustment in binder/filler ratio does affect the workability over time. As expected, the reduced BFS/LS ratio decreased the compressive strength of the hardened composite. The flexural strength was stable for all mixes the V-series but the deflection capacity significantly reduces for the lowest BFS/LS ratio.
- Reducing the SF/CEM I (X-series) ratio strongly affects all the studied mechanical properties. The slump flow diameter clearly reduced with decreasing SF/CEM I ratio, as did the compressive strength. In the 4-point bending test, a lower SF/CEM I ratio resulted in an increase of flexural deflection capacity and therewith the maximum flexure strength also increased. Thus, this parameter has proven to be very effective for finetuning both fresh and hardened mechanical properties.
- The increase in W/S (L-series) ratio resulted in a reduction of the compressive and flexural strength, however it did not affect the flexural deflection capacity. As expected, the change in W/S ratio did strongly impact the slump flow diameter, with an increase of ± 4% per 0.01 increase of W/S ratio.
- Interestingly, the reduction of the additives (L-series) did influence the mechanical properties of the material. A decrease in compressive strength and a small increase in deflection capacity was found. As expected, the reduction of the VMA and SP in similar proportions did not lead to any significant change in workability.

3.5. Material selection for Phase 2

Based on the research conducted in Phase 1, Mix X_3 and Mix L_4 were selected for further investigation into their fresh and hardened properties. Both mixes show good flexural properties in combination with a compressive strength of ± 40 MPa and improved workability. However, when looking in detail, the differences in the mechanical properties are quite pronounced, which makes it relevant to compare them under printing conditions. Where Mix X_3 displayed a relatively high compressive and flexural strength (43.6 MPa and 10.84 MPa) in combination with a very low associated standard deviation, Mix L_4 performed optimal in the flexural deflection capacity (11.91 mm) but showed significantly lower compressive and flexural strength (38.6 MPa and 9.02 MPa). And even though the two mixtures both display a larger slump flow diameter than Mix A, the difference in diameter between Mix X_3 and Mix L_4 is still significant (~10%). An overview of the mechanical test results, including the flexural stress - deflection curves from the 4-point bending test, can be found in Figs. 11–13.

In the continuation of this paper, Mix X_3 will be referred to as Mix C, and Mix L_4 will be referred to as Mix D.

4. Results and discussion Phase 2

4.1. Unconfined uniaxial compression test

The evolution of the compressive strength over time has been acquired by performing the UUCT at various time intervals. The outcomes for Mix C and Mix D, together with their trendline and that of the original Mix A, are presented in Fig. 14. The apparent Young's moduli were calculated by post-processing the fresh state compression stress values and the associated strain. The results can be seen in Fig. 15. The linear trendlines for Mix A, Mix C and Mix D are represented Table 6. The parameter t is specified in minutes.

As expected from the slump flow test results, Mix C and Mix D have a reduced fresh compressive strength and apparent Young's modulus compared to Mix A. This indicates that they may perform better in the pumping phase of the printing routine but will probably have lower buildability. Besides the overall lower values, Fig. 15 reveals that Mix C and Mix D have a significantly slower Young's modulus development

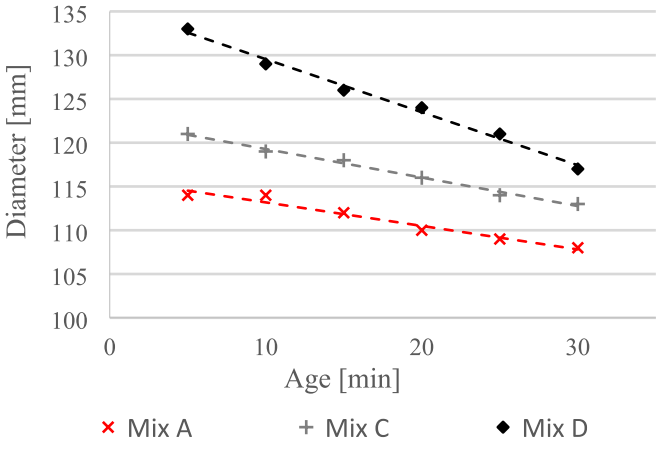

Fig. 11. Slump flow Diameter of Mix A, C and D.

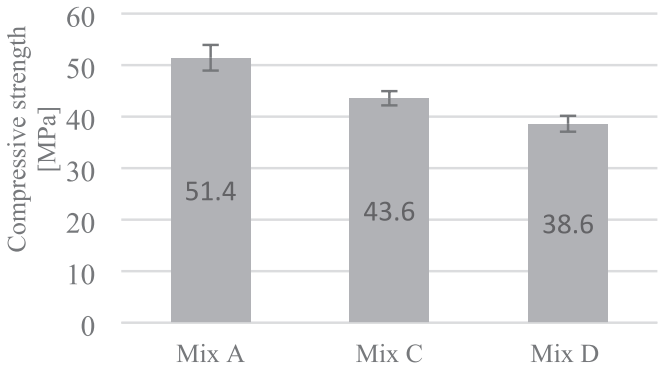

Fig. 12. Cast compressive strength of Mix A, C and D.

over time compared to Mix A. The same observation can be made for the compressive strength, only here, due to the high scatter of the results, the difference is not as pronounced. This can be related to the strongly reduced binder to filler ratio of Mix C and Mix D compared to mix A.

The linear trendlines, together with the printing parameters (i.e., print speed, wall length, layer width and layer height) are used in the model proposed by Suiker [53] to predict the achievable building height during printing. For Mix C this results in an estimated building height of 13 layers, after which failure will occur due to elastic buckling. Buckling failure is also the predicted failure mode for Mix D, but here failure is expected to occur already after 10 layers.

4.2. Buildability test and print quality assessment

Both Mix C and Mix D have successfully been printed at the TU/e. Prior to printing, a nozzle speed test was carried out on the selected mixtures to determine the printing speed for optimal shape retention of the layer. Based hereon, Mix C and Mix D were printed with a nozzle speed of 33 and 30 mm/s, respectively.

Mix C showed good print quality, with consistent material flow and stable layer shape, as can be seen in Fig. 16. The mixture showed excellent buildability and achieved a height of 23 layers, after which the wall failed due to elastic buckling.

The pumpability of Mix C, when used with the M−tech P20 pump, presented certain challenges. One of the issues observed was arching of the material within the pump reservoir. This arching phenomenon hindered the smooth flow of the material towards the Archimedes transport screw and into the rotor–stator, thus not fulfilling the full pumpability requirement, despite the good print quality after extrusion. It is worth noting that the slump flow table tests results displayed in section 3.1 had already indicated that Mix C (there referred as Mix X_3) did not meet the requirements for minimal flow conditions, as proposed by Cho et al. [39].

Throughout the printing session, including the printing of the

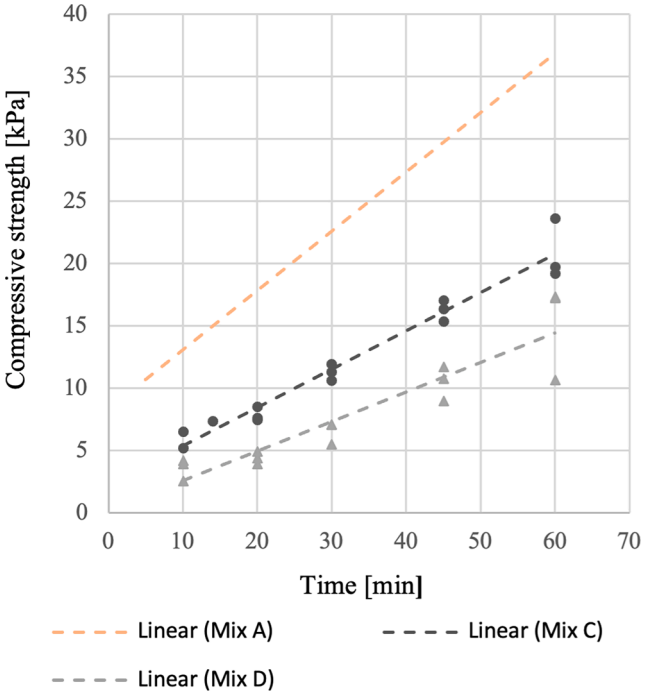

Fig. 14. Fresh compressive strength development over time.

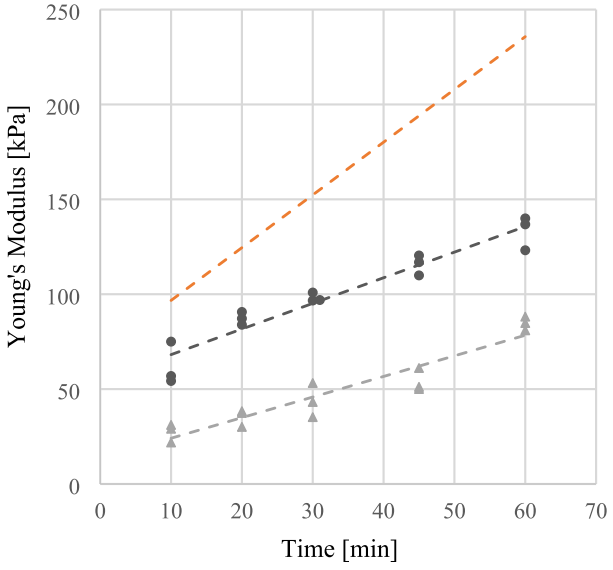

Fig. 15. Development of the fresh apparent Young's Modulus development over time.

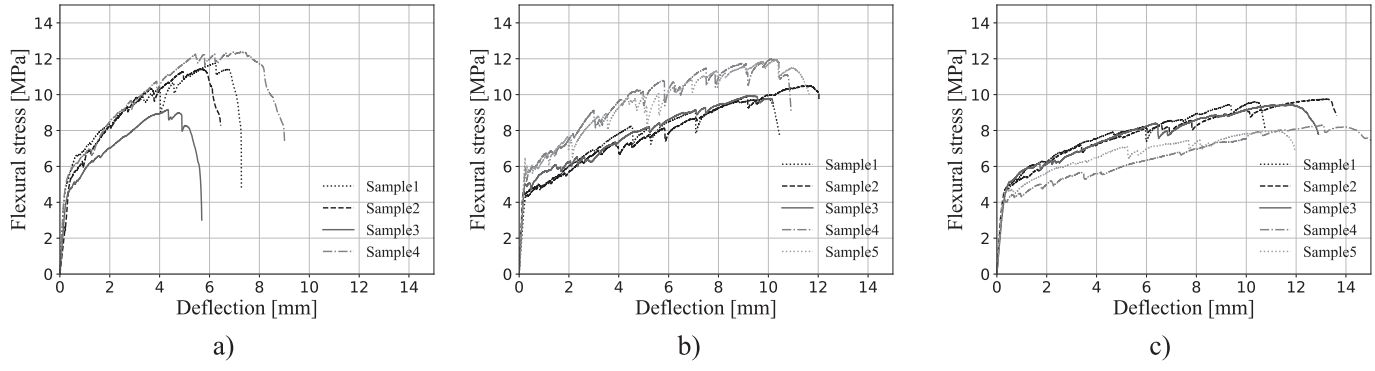

Fig. 13. Flexural stress - Deflection curves of the cast samples of (a) Mix A, (b) Mix C and (c) Mix D.

Table 6
Linear trendline equations derived from UUCT.

	$\sigma_c(t)[Pa]$	$E(t)[kPa]$
Mix A	$0.49t + 8.04$	$2.89t + 66.26$
Mix C	$0.31t + 2.27$	$1.35t + 54.66$
Mix D	$0.24t + 0.21$	$1.09t + 13.25$

additional beams, Mix D presented very good pumpability. This is in accordance with the findings in section 3.1, where Mix D (Mix L_4) complied with the minimal flow diameter as described by Cho et al [39]. Furthermore, it showed good extrudability and constant material flow. However, the buildability of Mix D was somewhat lower than that of Mix C, which is in correspondence with the UUCT results. The wall failed due to elastic buckling during the printing of the 15th layer, as can be observed in Fig. 17.

When we compare the actual buildability height with the expected buildability height that was retrieved from the unconfined uniaxial compression test using Suiker's model [53], we find that both Mix C and Mix D perform significantly better (77% and 50%, respectively) than predicted. This result was also previously found for Mix A [17], and it is expected that this is due to additional stiffening of the material during pumping and extrusion. Note, again, that the model uses UUCT results as input, and these tests are performed on cast, not printed, samples.

4.3. Compression test

The results of the compression tests, as illustrated in Fig. 18, indicate that the average compressive strength of the printed samples tested in orientation ***v*** was 5% higher than that of samples tested in orientation ***w***. Furthermore, it was observed that the compressive strengths of the printed samples were superior to those of the cast samples (shown in Fig. 12). This trend was particularly pronounced for Mix D, where the compressive strength increased from 38.6 MPa for cast to 41.2 MPa for printed in orientation ***w*** and 43.6 MPa in orientation ***v***. This finding is in contradiction with research conducted on mixtures without fibre reinforcement where a reduction in compressive strength is often reported for printed samples in respect to cast samples [57,58]. However, research on 3DP-SHCC samples have more often shown a higher compressive strength for the printed samples [15,17,19].

One possible explanation for enhanced compressive strength is the potential mix compaction during the printing process. In the process of pumping the material through the printing hose and additionally squeezing the mixture through a nozzle it is plausible that the material can get further compacted. This could also account for the increased buildability performance that was observed for both mixtures.

4.4. 4-point bending test

The 4-point bending tests were conducted on the printed samples of Mix C and D in the orientation ***v.u***. The flexural stress - deflection curves of these tests are shown in Fig. 19. The printed samples of Mix C and Mix D demonstrate a significant improvement in deflection capacity when compared to Mix A, showing increases of 59% and 239%, respectively. Despite this significant improvement, the average maximum flexural stress remains approximately constant for all three printed materials, around 8.5 MPa.

Simultaneously, it stands out that the cast composites have a higher flexural strength and a higher associated ductility (see Fig. 13 and Table 7) compared to their printed counterparts. The average flexural strength of the printed samples was reduced by 25.1% and 6.2% for Mix C and Mix D, respectively. The average values for the deflection at maximum stress with 3.41 mm and 5.25 mm provide an even bigger reduction of 65.4% and 55.9%. During the early flexural behavior, the printed materials exhibit a higher flexural stress at first crack, approximately 10% higher than the cast materials. Additionally, the deflection at first crack in the printed composites is significantly lower. These two observations suggest that the matrices of the printed composites have a higher E-modulus, indicating increased stiffness in comparison to the cast composites.

The flexural toughnesses, T_{LOP} and T_{MOR}, presented in Table 7, were computed to assess the overall performance of the six composites. The results of T_{LOP} indicate that the energy stored in the materials up to the point of non-linearity shows a small but significant reduction for the printed composites. This is in line with the hypothesis that the matrices of the printed composites have higher E-modulus. The impact of the printing process on the different composites becomes redundantly clear when reviewing the values of T_{MOR}. Where the energy storage capacity is reduced with 70, 72 and 76 percent, for Mix A, Mix C and Mix D respectively.

Overall, it can be concluded that the alterations made in Phase 1 resulted in improved performance under flexural loading. Mix C and Mix D out-perform the original Mix A both in the cast and printed form.

4.5. Uniaxial tensile test

The uniaxial tensile tests were conducted on cast and printed samples of both Mix C and Mix D. The stress–strain curves acquired from these tests are presented in Fig. 20 for the cast samples and in Fig. 21 for the samples that were extracted from the printed beams. The figures present only the curves of the samples where the final fracture occurred within the reduced cross-sectional area (see Fig. 8), therefore the number of samples shown per mixture varies. In Table 8 the average values with the associated standard deviation are shown for all four composites.

The findings obtained from the cast composites indicate that Mix D surpasses Mix C concerning both tensile strength (29%) and strain

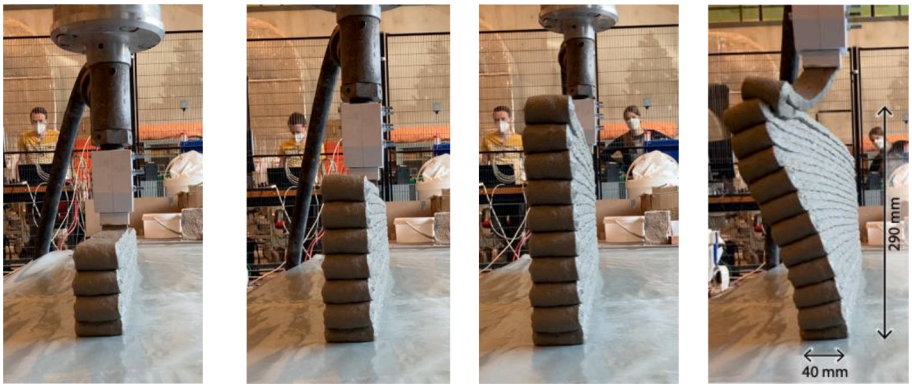

Fig. 16. Buildability test Mix C, failure after 23 layers.

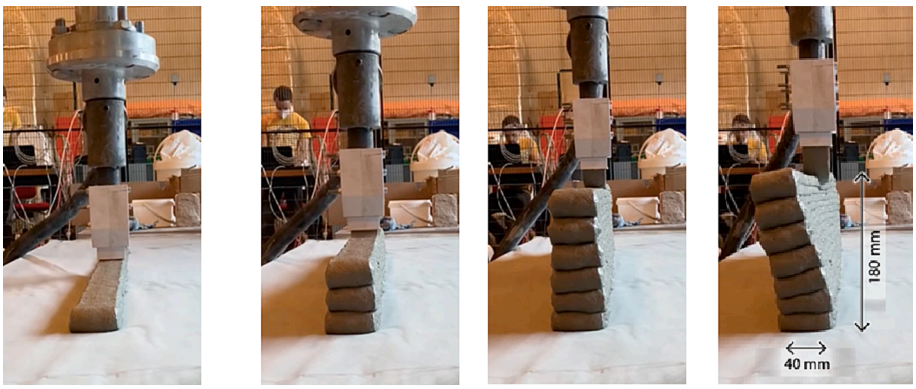

Fig. 17. Buildability test Mix D, failure after 15 layers.

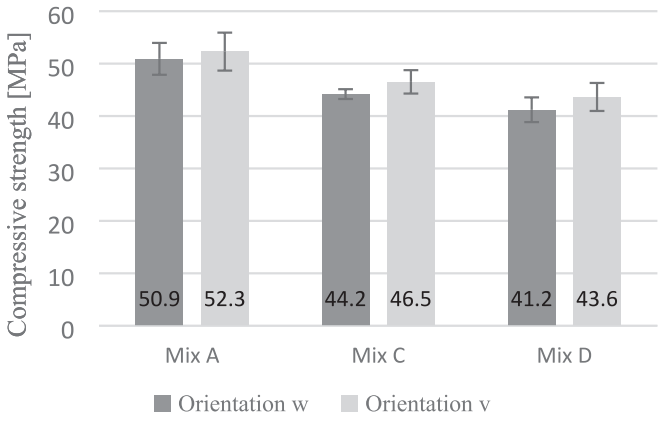

Fig. 18. Compressive strength results (with standard deviation) of Mix A, C and D in orientation w and orientation v.

hardening capacity (62%). For the printed composites no significant difference was found in the tensile strength, however, Mix D still performs better in terms of final strain (64%). It is important to note that the cast material consistently exhibits superior strain hardening performance compared to the printed material. Specifically, when printed, Mix C experiences a reduction in tensile strain by 38%, and Mix D experiences a reduction of 37%.

The tensile toughness max tensile stress ($T_{t,MOR}$), which represents the energy absorption capacity per unit volume, was calculated for all four composites. The tensile toughness is an important indicator when assessing the efficiency of strain hardening cementitious composites [47]. The values demonstrate the superior strain hardening capacity of Mix D in comparison with Mix C. In the case of cast composites, Mix D exhibits more than double the tensile toughness of Mix C, while for the printed samples, Mix D displays 33% higher energy storage capacity.

As with the flexural toughness a reduction of the tensile toughness of 42% (Mix C) and 56% (Mix D) was found for the printed composites.

From the shape of the stress–strain curves it can be observed that Mix D, both cast and printed, has a stable slope throughout the tensile test. This indicates a proper fibre/matrix interlayer bond and results in the stability of cracks that are formed during the cracking phase [1]. After the crack is formed the fibres effectively distribute the load from the crack plane back into the matrix and cause the formation of another crack at a similar or slightly higher tensile stress. On the other hand, the printed samples of Mix C show stress–strain curves with clear signs of unstable cracks.

From theory it is known that the number of cracks and the

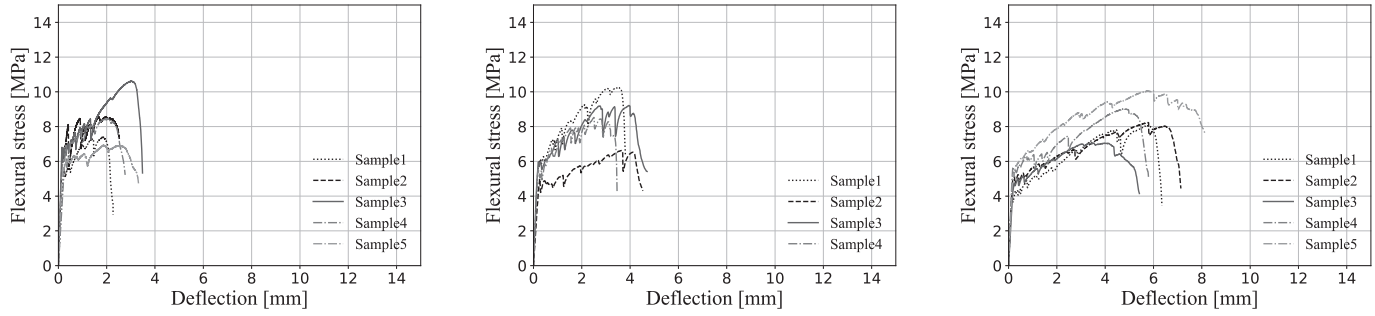

Fig. 19. Flexural stress - deflection curves for a) Mix A, b) Mix C and c) Mix D.

Table 7
Average results with standard deviations of the 4-point bending tests in phase 2.

		Flexural stress at first crack [MPa]		Deflection at first crack [%]		Maximum flexural stress [MPa]		Deflection at max flexural stress [%]		$T_{f,LOP}$ [Nm (x10^{-2})]		$T_{f,MOR}$ [Nm (x10^{-2})]	
Cast	***Mix A***	**5.37**	± 0.43	**0.34**	± 0.04	**11.18**	± 1.41	**5.80**	± 1.13	**1.45**	± 0.22	**81.0**	± 25.1
	Mix C	**5.28**	± 0.89	**0.31**	± 0.07	**10.83**	± 1.07	**9.85**	± 0.38	**1.27**	± 0.13	**136.6**	± 19.6
	Mix D	**4.90**	±0.42	**0.36**	± 0.04	**9.02**	± 0.81	**11.91**	± 1.25	**1.40**	± 0.08	**235.7**	± 34.2
Printed	***Mix A***	**5.89**	± 0.57	**0.23**	± 0.03	**8.68**	± 1.57	**2.14**	± 0.49	**1.09**	± 0.21	**24.3**	± 9.2
	Mix C	**5.69**	± 0.59	**0.25**	± 0.06	**8.66**	± 1.53	**3.41**	± 0.63	**1.15**	± 0.29	**37.9**	± 10.5
	Mix D	**5.31**	± 0.52	**0.30**	± 0.08	**8.49**	± 1.13	**5.25**	± 0.86	**1.26**	± 0.16	**56.4**	± 17.2

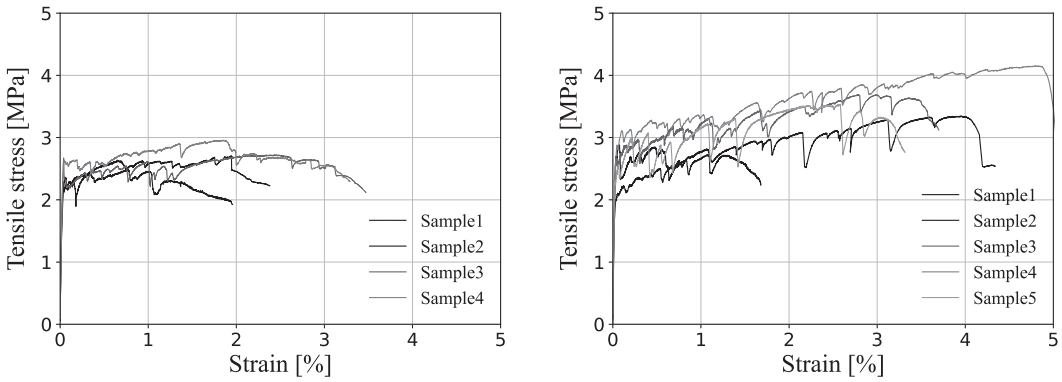

Fig. 20. Tensile stress – strain curves of the cast samples a) Mix C b) Mix D.

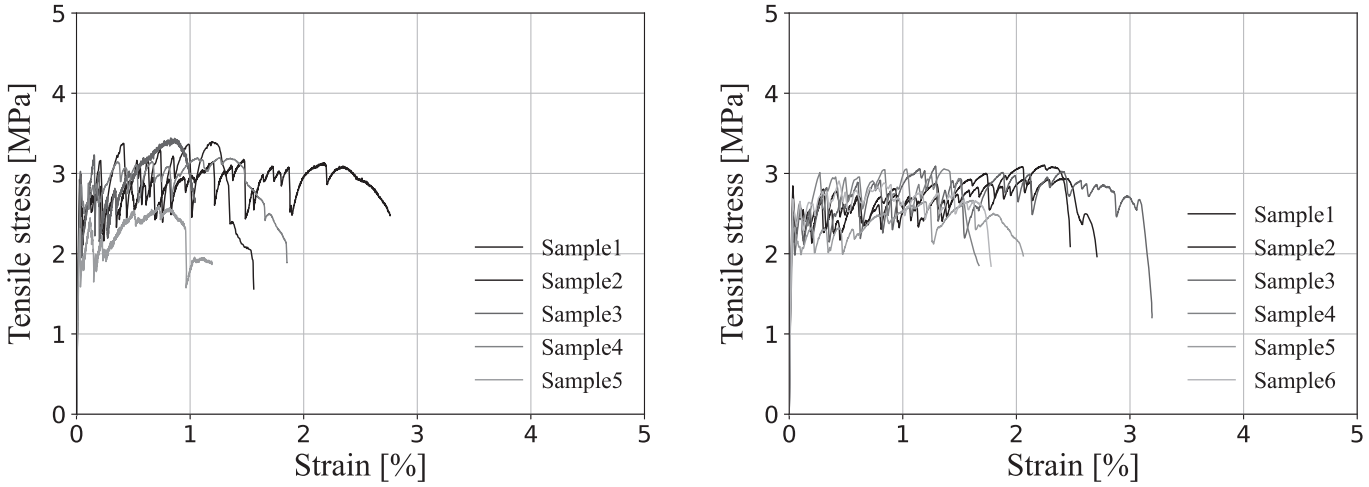

Fig. 21. Tensile stress – strain curves of the printed samples a) Mix C b) Mix D.

Table 8
Average results with standard deviations of the uniaxial tensile tests.

		Tensile stress at first crack [MPa]		**Tensile strain at first crack** [%]		**Maximum tensile stress** [MPa]		**Strain at max. tensile strength** [%]		$T_{t,MOR}$ [N*mm2]		**Cracks** [-]
Cast	***Mix C***	2.51	± 0.20	0.043	± 0.007	2.72	± 0.19	1.75	± 0.70	4.45	± 1.86	11 ± 3
	Mix D	2.40	± 0.43	0.028	± 0.011	3.52	± 0.47	2.84	± 1.79	9.15	± 6.2	20 ± 4
Printed	***Mix C***	2.61	± 0.25	0.031	± 0.006	3.16	± 0.34	1.09	± 0.31	3.04	± 1.03	7 ± 2
	Mix D	2.48	± 0.12	0.029	± 0.013	2.97	± 0.18	1.79	± 0.52	4.06	± 1.94	13 ± 3

Fig. 22. Representative samples for the cracking patterns of the tested mixes.

distribution of these cracks is closely associated with the tensile strain capacity of the composite [2]. After analyses of the crack patterns, it was concluded that the printed Mix C samples displayed a smaller number of cracks and that these were more localized over the length of the reduced cross-sectional area. Where the crack patterns of Mix D, both cast and printed, were evenly dispersed throughout the reduced cross-section (see Fig. 22), in accordance with the observation made from the stress–strain curves.

Furthermore, it can be concluded that the printed composites developed fewer cracks in comparison to the cast counterparts. For both Mix C and Mix D the number of cracks was reduced with ± 35%.

In early publications on 3DP-SHCC, the general consensus was that printed SHCC elements performed better than cast elements under tensile loading due to the favourable alignment of fibres [14,16,59]. However, a recent publication of Zhou et al. [60] reported lower tensile strength and strain capacity after printing of 10% and 25%, depending on the printing parameters. The primary reasons for the reduction in the mechanical properties are proposed to be unfavourable fibre orientation and pore distribution due to the pumping system. In a previous publication of the authors [17], loss in tensile strength and strain capacity was observed as well, and also here the effect of the pumping system on the material properties was proposed as a plausible explanation.

5. Conclusion

This study set out to improve the printability and strain hardening capacity of a previously developed 3DP-SHCC mix composition by altering multiple parameters. Indeed, for two 3DP-SHCC designs (Mix C and D), significant improvements in strain-hardening capacity were achieved while printability was also improved. From the conducted research, the following conclusions can be drawn:

- For the development of 3DPC-SHCC, the Silica fume content and the W/S ratio are relevant parameters to simultaneously optimize fresh and strain hardening properties.
- The study highlights the importance of tailoring the initial stiffness for optimizing pumpability and avoiding issues like arching as observed for Mix C.
- The printing sessions of the two developed mix designs confirm the applicability of the minimal slump flow diameter criteria proposed by Cho et al. [39] for 3D printable SHCC.
- The extrudability requirements were met by both developed mix designs, resulting in a good print quality with a stable layer shape and without extrusion flaws such as tearing and overprinting.
- The buildability performance of Mix C and Mix D exceed the expectations derived from the UUCT test. Both mix designs are sufficiently buildable and have elastic buckling as main failure mechanism.
- The reduction of the matrix density and matrix strength to decrease the fibre/matrix interlayer bond has proven to be a good approach to improve the energy balance of SHCC and to satisfy the energy requirement.
- Mechanical properties measured using cast and printed samples of the same mixture are different. On the one hand, the hardened mechanical strength (flexural and tensile) and strain capacity (in bending and in tension) are reduced in printed compared to cast samples; on the other hand, the buildability test and unconfined uniaxial compression test resulted in higher values for green strength and compressive strength.

The presented research makes clear that the printing process influences the material and mechanical properties of the SHCC, and this can have implications on the structural integrity of printed elements when they are designed based on casted mechanical properties. However, currently there are no established codes or national standards for the designing and testing of printed concrete elements and materials. Existing codes, such as NEN-EN-206, are not applicable in this context, as they do not account for the unique characteristics of printed elements, namely the lack of compaction (vibration) during printing and the anisotropic nature resulting from the layered build-up. As a result, the development of printed load-bearing structures, demands a comprehensive preliminary experimental investigation to provide robust support for the structural design throughout all its phases [61]. The industry thus relies on conducting structural tests on 3D printed prototypes [7] to verify the structural integrity of printed elements. This approach would also apply for load bearing elements printed with fibre-reinforced concretes or SHCCs.

Nevertheless, the impact of the printing process on the mechanical properties of 3DP-SHCC is a relevant and interesting subject for future investigation. To comprehend the influence of the printing process, research into the effect of specific printing phases on the mechanical properties is recommended. This approach will facilitate the identification of the principal bottleneck within the printing process concerning SHCC. In continuation, research can be conducted on the influence of the crucial printing phase on the composite's microstructure, to understand the specific changes and how these may be overcome.

CRediT authorship contribution statement

A.L. van Overmeir: Conceptualization, Data curation, Formal analysis, Investigation, Methodology, Software, Visualization, Writing – original draft, Writing – review & editing. **B. Šavija:** Writing – review & editing, Supervision, Methodology. **F.P. Bos:** Funding acquisition, Resources, Supervision, Writing – review & editing. **E. Schlangen:** Writing – review & editing, Supervision, Resources.

Declaration of Competing Interest

The authors declare that they have no known competing financial interests or personal relationships that could have appeared to influence the work reported in this paper.

Data availability

Data will be made available on request.

Acknowledgement

This research was funded through the NWO Open Technology Program, project 'High Performance 3D Concrete Printing', grant number 17251. Special thanks go out to Professor G. van Zijl, for providing constructive feedback in the final writing stage.

References

[1] V.C. Li, On engineered cementitious composites (ECC), J. Adv. Concr. Technol. 1 (3) (2003) 215–230.
[2] V. Li, Engineered Cementitious Composites (ECC), Springer, 2019.
[3] D. Asprone, C. Menna, F. Bos, T. Salet, J. Mata-Falcónd, W. Kaufmannd, Rethinking reinforcement for digital fabrication with concrete, Cem. Concr. Res. 112 (2018) 111–121.
[4] T. Wangler, E. Lloret, L. Reiter, N. Hack, F. Gramazio, M. Kohler, M. Bernhard, B. Dillenburger, J. Buchli, N. Roussel, R. Flatt, Digital concrete: opportunities and challenges, RILEM Technical Letters 1 (2016) 67–75.
[5] R.A. Buswell, W.R. Leal de Silva, S.Z. Jones, J. Dirrenberger, 3D printing using concrete extrusion: A roadmap for research, Cem. Concr. Res. 112 (2018) 37–49.
[6] G. De Schutter, K. Lesage, V. Mechtcherine, V.N. Nerella, G. Habert, I. Agusti-Juan, Vision of 3D printing with concrete; Technical, economic and environmental potentials, Cem. Concr. Res. 112 (2018) 25–36.
[7] T. Salet, Z. Ahmed, F. Bos, H. Laagland, Design of a 3D printed concrete bridge by testing, Virtual Phys. Prototyping 13 (3) (2018) 222–236.
[8] S. Lim, R. Buswell, T. Le, S. Austin, A. Gibb, T. Thorpe, Developments in construction-scale additive manufacturing processes, Autom. Constr. 21 (2012) 262–268.
[9] Z. He, J. Chen, Z. Liu, Z. Ma, Analytical approach for bursting cracking analysis of post-tensioned anchorage zone, Structures 52 (2023) 401–409.

[10] L. Hass, F. Bos, T. Salet, Characterizing the bond properties of automatically placed helical reinforcement in 3D printed concrete, Constr. Build. Mater. 355 (2022), 129228.
[11] Y. Chen, J. Yu, H. Younas, C. Leung, Experimental and numerical investigation on bond between steel rebar and high-strength Strain-Hardening Cementitious Composite (SHCC) under direct tension, Cem. Concr. Compos. 112 (2020), 103666.
[12] M. Deng, J. Pan, H. Sun, Bond behavior of steel bar embedded in Engineered Cementitious Composites under pull-out load, Constr. Build. Mater. 168 (2018) 705–714.
[13] L. Hass, K. Nefs, F. Bos, T. Salet, Application potential of combining strain hardening cementitious composites and helical reinforcement for 3D concrete printed structures: case study of a spiral staircase, Building and Construction Materials vol. Under review (2023).
[14] D.G. Soltan, V.C. Li, A self-reinforced cementitious composite for building-scale 3d printing, Cem. Concr. Compos. 90 (13) (2018) 1–13.
[15] S.C. Figueiredo, C.R. Rodriguez, Z.Y. Ahmed, D. Bos, Y. Xu, T. Salet, O. Çopuroglu, E. Schlangen, F.P. Bos, An approach to develop printable strain hardening cementitious composites, Mater. Des. 169 (2019), 107651.
[16] H. Ogura, V. Nerella, V. Mechtcherine, Developing and testing of strain-hardening cement-based composites (shcc) in the context of 3d-printing, Materials 11 (8) (2018) 1–18.
[17] A. van Overmeir, S. Figueiredo, B. Šavija, F. Bos, E. Schlangen, Design and analysis of printable SHCC with optimized particle size distribution, Constr. Build. Mater. 324 (2022), 126411.
[18] V.C. Li, et al., On the emergence of 3d printable engineered, strain hardening cementitious composites (ECC/SHCC), Cem. Concr. Res. 132 (2020), 106038.
[19] S.C. Figueiredo, C.R. Rodriguez, Z.Y. Ahmed, D. Bos, Y. Xu, T. Salet, O. Çopuroglu, E. Schlangen, F. Bos, Mechanical Behavior of Printed Strain Hardening Cementitious Composites, Materials 13 (10) (2020) 2253.
[20] J. Zhou, S. Qian, M.G. Sierra Beltran, G. Ye, K. van Breugel, V.C. Li, Development of engineered cementitious composites with limestone powder and blast furnace slag, Mater. Struct. 43 (6) (2010) 803–814.
[21] S.W. Khan, M. Kamal, F.A. Khan, A. Gul, M. Alam, F. Shah, K. Shahzada, Performance evaluation of the fresh and hardened properties of different PVA-ECC mixes: An experimental approach, Case Stud. Constr. Mater. 18 (2023) e01764.
[22] Z. Pan, C. Wu, J. Liu, W. Wang, J. Liu, Study on mechanical properties of cost-effective polyvinyl alcohol engineered cementitious composites (PVA-ECC), Constr. Build. Mater. 78 (2015) 397–404.
[23] A. Drescher, A. Waters, C. Rhoades, Arching in hoppers: I. Arching theories and bulk material flow properties, Powder Technol. 84 (2) (1995) 165–174.
[24] G. Enstad, A novel theory on the arching and doming in mass flow hoppers, Norwegan technical university (1981).
[25] R. Buswell, J. Xu, D. De Becker, J. Dobrzanski, J. Provis, J. Kolawole, P. Kinnell, Geometric quality assurance for 3D concrete printing and hybrid construction manufacturing using a standardised test part for benchmarking capability, Cem. Concr. Res. 156 (2022), 106773.
[26] H. Zhang, J. Wang, Y. Liu, X. Zhang, Z. Zhao, Effect of processing parameters on the printing quality of 3D printed composite cement-based materials, Mater. Lett. vol. 308, no. Part B (2022), 131271.
[27] D. Dinger, J. Funk, Predictive process control of crowded particulate suspensions: Applied to ceramic manufacturing, Springer, Boston, 1994.
[28] S. Bhattacherjee, S. Jain, M. Santhanam, Developing 3D printable and buildable limestone calcined clay-based cement composites with higher aggregate content, Constr. Build. Mater. 376 (2023), 131058.
[29] C. Zhang, V. Nerella, A. Krishna, S. Wang, Y. Zhang, V. Mechtcherine, N. Banthia, Mix design concepts for 3D printable concrete: A review, Cem. Concr. Compos. 122 (2021), 104155.
[30] C. Ferraris, K. Obla, R. Hill, The influence of mineral admixtures on the rheology of cement paste and concrete, Cem. Concr. Res. 31 (2) (2001) 245–255.
[31] Z. Geng, W. She, W. Zuo, K. Lyu, H. Pan, Y. Zhang, C. Miao, Layer-interface properties in 3D printed concrete: Dual hierarchical structure and micromechanical characterization, Cem. Concr. Res. 138 (2020), 106220.
[32] C. Liu, X. Wang, Y. Chen, C. Zhang, L. Ma, Z. Deng, C. Chen, Influence of hydroxypropyl methylcellulose and silica fume on stability, rheological properties, and printability of 3D printing foam concrete, Cem. Concr. Compos. 122 (2021), 104158.
[33] R. Banar, P. Dashti, A. Zolfagharnasab, A. Ramezanianpour, A. Ramezanianpour, A comprehensive comparison between using silica fume in the forms of water slurry or blended cement in mortar/concrete, J. Build. Eng. 46 (2022), 103802.
[34] M. Ashraf, M. Iqbal, M. Rauf, M. Ashraf, A. Ulhaq, H. Muhammad, Q. Liu, Developing a sustainable concrete incorporating bentonite clay and silica fume: Mechanical and durability performance, J. Clean. Prod. 337 (2022), 130315.
[35] M. Hou, D. Zhang, V. Li, Crack width control and mechanical properties of low carbon engineered cementitious composites (ECC), Constr. Build. Mater. 348 (2022), 128692.
[36] M.o. Li, V.C. Li, Rheology, fiber dispersion, and robust properties of Engineered Cementitious Composites, Mater. Struct. 46 (3) (2013) 405–420.
[37] D. Marchon, S. Kawashima, H. Bessaies-Bey, S. Mantellato, S. Ng, Hydration and rheology control of concrete for digital fabrication: Potential admixtures and cement chemistry, Cem. Concr. Res. 112 (2018) 96–110.
[38] EN_1015-3, "Methods of test for mortar for masonry. Determination of consistence of fresh mortar (by flow table)," European, Standard, 1999.
[39] S. Cho, J. Kruger, F. Bester, M. van den Heever, A. van Rooyen, G. van Zijl, A Compendious Rheo-Mechanical Test for Printability Assessment of 3D Printable Concrete. Rilem International conference on concrete and digital fabrication, 2020.
[40] S. Shamir, S. Raman, A. Kaish, A.M. Azrul, Calibration of ASTM C230 Cone for Measuring Flow Diameter of Self-flowing Mortar According to the EFNARC Recommendation. Rheology and Processing of Construction Materials, Dresden, 2020.
[41] N. Roussel, P. Coussot, Fifty-cent rheometer'' for yield stress measure-ments: From slump to spreading flow, J. Rheol. 49 (3) (2005) 705–718.
[42] T. Shin, J. Kim, First step in modelling the flow table test to characterize the rheology of normally vibrated concrete, Cem. Concr. Res. 152 (2022), 106678.
[43] A. International, "ASTM-C39: Standard Test Method for Compressive Strength of Cylindrical Concrete Specimens," www.ASTM.org, 2017.
[44] V. Mechtcherine, K.V. Tittelboom, F.P. Bos, et al., A roadmap for quality control of hardening and hardened printed concrete, Cem. Concr. Res. 157 (2022), 106800.
[45] D. Kim, A. Naaman, S. El-Tawil, Comparative flexural behavior of four fiber reinforced cementitious composites, Cem. Concr. Compos. 30 (10) (2008) 917–928.
[46] K. Turk, M. Nehdi, Flexural toughness of sustainable ECC with high-volume substitution of cement and silica sand, Constr. Build. Mater. 270 (2021), 121438.
[47] B. Tahmouresi, P. Nemati, M. Asadi, A. Saradar, M. Moein, Mechanical strength and microstructure of engineered cementitious composites: A new configuration for direct tensile strength, experimental and numerical analysis, Constr. Build. Mater. 269 (2021), 121361.
[48] R. Wolfs, A. Suiker, Structural failure during extrusion-based 3D printing processes, Int. J. Adv. Manuf. 104 (1–4) (2019) 564–584.
[49] ASTM_D2166-00, "Standard Test Method for Unconfinned Compressive Strength of Cohesive Soil," www.astm.org, 2000.
[50] F. Bos, P. Kruger, S. Lucas, G.V. Zijl, Juxtaposing fresh material characterisation methods for buildability assessment of 3D printable cementitious mortars, Cem. Concr. Compos. 120 (2021), 104024.
[51] B. Panda, J. Lim, M. Tan, Mechanical properties and deformation behaviour of early age concrete in the context of digital construction, Compos. B Eng. 165 (2019) 563–571.
[52] U. Pott, C. Wolf, Y. Petryna, D. Stephan, Evaluation of the unconfined uniaxial compression test to study the evolution of apparent printable mortar properties during the early age transition regime, Cem. Concr. Res. 161 (2022), 106956.
[53] A. Suiker, Mechanical performance of wall structures in 3d printing processes: theory, design, tools and experiments, Int. J. Mech. Sci. 137 (1) (2018) 145–170.
[54] J. Kruger, S. Zeranka, G. van Zijl, 3d concrete printing: A lower bound analytical model for buildability performance quantification, Autom. Constr. 106 (2019), 102904.
[55] F. Bos, R. Wolfs, T. Salet, Z. Ahmed, Additive manufacturing of concrete in construction: potentials and challenges of 3D concrete printing, Virtual and Physical Prototyping 11 (3) (2016) 209–225.
[56] A. L. van Overmeir and A. L. van Overmeir, "Designing an interlayer reinforcement solution for printable strainhardening cement-based composites"," Delft University of Technology, Master's thesis, 2020. Retrieved from: https://repository.tudelft.nl/islandora/object/uuid%3A3e397363-4749-47e3-8f9a-201639ab74f2.
[57] R. Wolfs, F. Bos, T. Salet, Hardened properties of 3D printed concrete: The influence of process parameters on interlayer adhesion, Cem. Concr. Res. 119 (2019) 132–140.
[58] T. Le, S. Austin, S. Lim, R. Buswell, R. Law, A. Gibb, T. Thorpe, Hardened properties of high-performance printing concrete, Cem. Concr. Res. 42 (3) (2012) 558–566.
[59] K. Yu, W. McGee, T. Ng, H. Zhu, V. Li, 3D-printable engineered cementitious composites (3DP-ECC): fresh and hardened properties, Cem. Concr. Res. 143 (2021), 106388.
[60] W. Zhou, Y. Zhang, L. Ma, V. Li, Influence of printing parameters on 3D printing engineered cementitious composites (3DP-ECC), Cem. Concr. Compos. 130 (2022), 104562.
[61] F. Bos, M. Pradena, E. Kreiger, W. Silva, A. Rehman, D. Weger, R. Wolfs, Y. Zhang, L. Ferrara, V. Mechtcherine, The realities of additively manufactured concrete structures in practise, Cem. Concr. Res. 156 (2022), 106746.
[62] M. Deng, J. Pan, H. Sun, Bond behavior of steel bar embedded in Engineered Cementitious Composites under pullout load, Constr. Build. Mater. 168 (2018) 705–714.